Research Square

Preprints are preliminary reports that have not undergone peer review.
They should not be considered conclusive, used to inform clinical practice,
or referenced by the media as validated information.

Global submesoscale eddies driven by ocean mesoscale coherent structures

Nannan Zi
Aerospace Information Research Institute
Xiao-Ming Li
lixm@radi.ac.cn

Aerospace Information Technology University

Research Article

Keywords:

Posted Date: November 18th, 2026

DOI: https://doi.org/10.21203/rs.3.rs-11734194/v1

License: This work is licensed under a Creative Commons Attribution 4.0 International License.
Read Full License

Additional Declarations: The authors declare no competing interests.

Global submesoscale eddies driven by ocean mesoscale coherent structures

Nannan Zi [1, 2], Martin Gade [3], Ge Chen [4], Zhiwei Zhang [5], Chen Wang [6], Jianjun Liang [6], Zhiyou Jing [7], Xiao-Ming Li [6, 8 *]

1, Aerospace Information Research Institute, Chinese Academy of Sciences, Beijing, China
2, University of Chinese Academy of Sciences, Beijing, China
3, Universität Hamburg, Institut für Meereskunde, Hamburg, Germany
4, Department of Marine Technology, Ocean University of China, Qingdao, China
5, Frontier Science Center for Deep Ocean Multispheres and Earth System (FDOMES) and Physical OceanographyLaboratory/Key Laboratory of Ocean Observation and Information of Hainan Province, Sanya Oceanographic Institution, Ocean University of China, Qingdao/Sanya, China
6, Aerospace Information Technology University, Jinan, China
7, State Key Laboratory of Tropical Oceanography, South China Sea Institute of Oceanology, Chinese Academy of Sciences, Guangzhou, China
8, Hainan Aerospace Technology Innovation Center, Wenchang, China
Corresponding author E-mail address: lixm@radi.ac.cn (X.-M. Li)

Ocean submesoscale eddies, typically smaller than 50 km in spatial scales, play a pivotal role in the oceanic energy cycle and vertical transport of heat and nutrients, thereby regulating marine ecosystems and Earth's climate. However, their kilometer spatial scales have hindered systematic observation, limiting our understanding of these submesoscale features and their drivers on global scales. Here, we reveal the dominant role of mesoscale Lagrangian coherent structures (LCSs) in driving global submesoscale eddy generation based on spaceborne synthetic aperture radar augmented by radar altimeter data. It is found that 84% of submesoscale eddies are clustered within 10 km of mesoscale LCSs — regions exhibiting high kinetic energy and persistent strain. These LCSs primarily manifest in the form of mesoscale eddies, and nearly 50% of the submesoscale eddies occur within the ring-shaped areas spanning from 0.5 to 2 times the radius of the mesoscale eddies, where enhanced energy and strain are observed. The energy-strain enhancements in these submesoscale eddy hotspots suggest that the instabilities initiated by strain-induced frontogenesis dominate their generations. Our findings establish LCSs as key indicators for submesoscale activity, enabling global assessments of their contributions to energy balance and material transport.

Main

The global ocean is populated by ubiquitous rotating water masses with spatial scales ranging from a few meters to hundreds of kilometers, like weather systems in the atmosphere, known as ocean eddies **[Chelton et al., 2011; Holloway, 1986; Rai et al., 2025]**. Recently, the scientific and public attention has increasingly focused on smaller submesoscale eddies, with scales typically less than 50 km **[Munk et al., 2000; Su et al., 2018]**. These submesoscale eddies bridge mesoscale and small-scale dynamics, serving as pivotal conduits for both forward energy dissipation and inverse kinetic energy cascades **[Balwada et al., 2022; Schubert et al., 2020; Yu et al., 2024]**. Crucially, they exhibit strong vertical velocities of O (100 m d^{-1}), an order of magnitude larger than those associated with mesoscale eddies

(O (10 m d^{-1})) [Dong et al., 2025]. Such strong vertical velocities facilitate the exchange of nutrients and heat between surface and deep oceans, consequently fueling phytoplankton growth [Lévy et al., 2018], controlling upper ocean vertical heat transport [Su et al., 2018], and potentially inhibiting the El Niño-Southern Oscillation [Wang et al., 2022].

Submesoscale eddies have been found to be active under deep mixed-layer conditions during winter, and to be enhanced in regions with strong strain [McWilliams, 2016; Su et al., 2018; Zhang et al., 2021]. Moreover, they also preferentially occur in regions with prominent topographic features [Gula et al., 2016; Johannessen et al., 1996]. Based on these characteristics, it is argued that the mixed-layer instability [Callies et al., 2015], strain-induced frontogenesis [Lapeyre et al., 2006], and flow-topography interaction [Gula et al., 2016; Rosso et al., 2015] are likely important mechanisms responsible for the generation of submesoscale eddies. However, the small spatial scales of submesoscale eddies pose a challenge for global observations and numerical simulations, limiting the majority of studies to local or regional areas [Gula et al., 2016; Stuhlmacher and Gade, 2023; Zhang et al., 2021]. Despite extensive research on their generation mechanisms, the dominant mechanism remains controversial and appears to differ across regions, making it difficult to determine through regional investigations [McWilliams, 2016; Srinivasan et al., 2017].

Satellite altimeter already provides a powerful tool for global observations of mesoscale dynamics [Chelton et al., 2011; Chen and Han, 2019]. Based on gridded altimetry data, mesoscale coherent structures — characterized by well-defined boundaries — are found to be one of the most energetic features in the global ocean, primarily manifesting as fronts and eddies [Beron-Vera et al., 2008; Prants et al., 2014; Tian et al., 2022]. Their coherent boundaries are often associated with convergent flows, in which the strain rate is expected to be large [Peacock and Haller, 2013; Yu et al., 2024]. This implies that mesoscale coherent structures may play a significant role in the generation of submesoscale eddies. To identify these features, various methodologies have been proposed, among which Lagrangian approaches, identifying structures referred to as Lagrangian coherent structures (LCSs), yield more reliable coherent boundaries than those derived from Eulerian frameworks [Beron et al., 2013; Liu and Abernathey, 2023]. However, the spatial resolution (~ 0.25°) of gridded altimeter products generated by merging along-track measurements is insufficient to resolve submesoscale processes [Chelton et al., 2011]. In contrast to well-documented mesoscale dynamics, systematic global observations of submesoscale eddies are still fragmentary [Ancher et al., 2025]. More importantly, due to the lack of global observation at submesoscale, how and to what extent these LCSs drive the generation of submesoscale eddies on a global scale remains poorly understood and unquantified. Notably, spaceborne Synthetic Aperture Radar (SAR), as the imaging radar with two-dimensional imaging capability at meter spatial resolution, operating independently of daylight and weather conditions, has already become a crucial tool for observing submesoscale eddies [Bashmachnikov et al., 2020; Stuhlmacher et al., 2020; Zi et al., 2024]. Additionally, recent deep learning algorithms enable the processing of large numbers of SAR acquisitions for global submesoscale eddy study [Zi et al., 2024; Zi et al., 2025].

In this study, we conduct a global study of the submesoscale eddy generation mechanism leveraging more than three million spaceborne SAR images. In addition, in

synergy with radar altimeter data, we derive the co-occurring mesoscale LCSs, thereby revealing the primary role of mesoscale LCSs in driving submesoscale eddies in the global ocean.

Results

Global submesoscale eddies detected by SAR

A deep-learning system [Zi et al., 2024], which has demonstrated its robust generalization (effectiveness) under various/complex ocean conditions, was employed on the aggregated 3,195,148 SAR scenes from Sentinel-1 (S1) and Environment Satellite (EnviSat) satellites (**Fig. 1a and Supplementary Fig. 1**) to extract the geographic locations and sizes of eddies in the global ocean. Consequently, a total of 82,750 ocean eddies were detected (**Fig. 1b**), including manifestations due to wave-current interactions [Johannessen et al., 1996], spatial accumulations of surfactants [Munk et al., 2000], and ice floes [Johannessen et al., 1987] (**Fig. 1c-e**). Our results show that the detected ocean eddies are widely distributed in the World's oceans, with some regional hotspots (**Fig. 1b and Supplementary Fig. 2a**) such as the previously reported Mediterranean and Black Seas [Karimova, 2012; Stuhlmacher and Gade, 2023; Zi et al., 2024]. These regions are also characterized by active mesoscale variabilities revealed by satellite radar altimeter [Mkhinini et al., 2014; Zatsepin et al., 2003]. In contrast, lower eddy occurrences were found in regions of prevailing high wind speeds such as the "Roaring Forties", between 40°S and 60°S, where the strong winds prevent the accumulation of surfactants, thereby reducing the visibility of eddies in SAR imagery. Notably, the eddy occurrence exhibits a dramatic decrease in the equatorial band. This pattern is similar to that observed for mesoscale features, as the weakened geostrophic balance in the tropical ocean makes them less stable and short-lived [Chelton et al., 2011; Chen and Han, 2019].

To distinguish submesoscale eddies from overall detections, we calculated the first baroclinic Rossby radius of deformation, R_d, for global oceans. It marks the transition from geostrophic mesoscale dynamics to ageostrophic submesoscale dynamics, and hence, eddies with a radius smaller than the local R_d are defined as submesoscale eddies [McWilliams, 1985; Schaeffer et al., 2017]. The calculated R_d ranges from approximately 5 km in polar areas to about 300 km in the near-equatorial band (**Supplementary Fig. 2b**). The eddy radius distribution shows that more than 98% of the detected eddies have a radius of less than 25 km (**Fig. 1f**), suggesting that nearly all eddies detected by SAR could not be observed by traditional altimeter products with a coarse resolution of 0.25°. By comparing eddy radius with local R_d, approximately 75.07% of all detected eddies are classified as submesoscale eddies for our subsequent analyses.

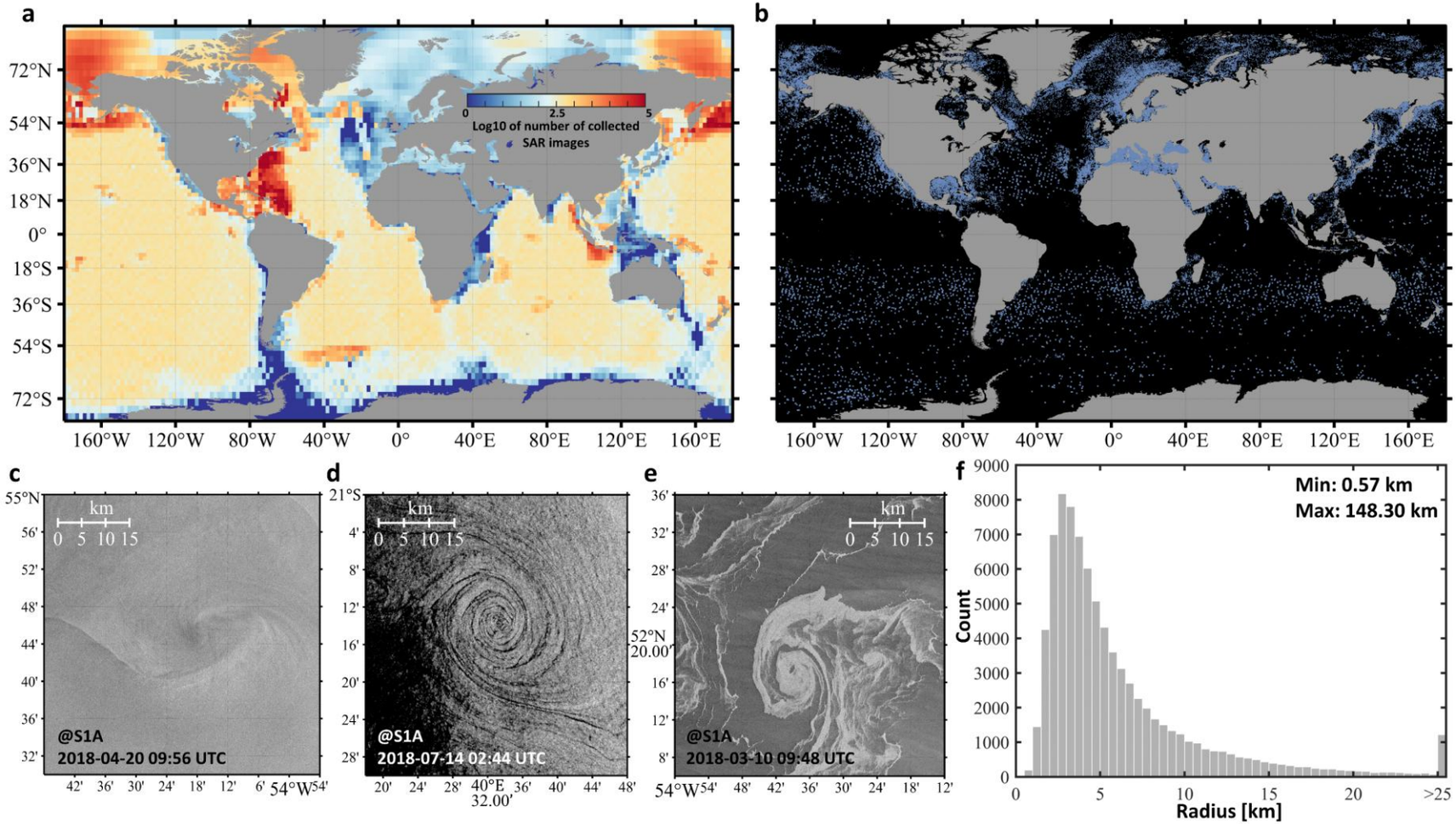


Fig. 1 | Global view of ocean eddies from high-resolution SAR observations. a, Spatial distribution of 3,195,148 S1 and EnviSat SAR images in $\log_{10}$ units counted on a 2° × 2° grid. Note that the uneven coverage patterns are largely due to satellite acquisition mode (**Supplementary Fig. 1**). **b**, Spatial distribution of the centers of 82,750 eddies detected using a deep-learning eddy detection system (**Methods**). **c-e**, Manifestations of eddies on SAR images due to wave-current interactions (**c**), accumulation of surfactants (**d**), and redistribution of ice floes (**e**). **f**, Eddy radius histogram, with the minimum and maximum radius being approximately 0.57 km and 148.30 km, respectively.

Drivers of global submesoscale eddy generation

The observed spatial similarity between submesoscale eddies and mesoscale features potentially points to a generation mechanism driven by mesoscale strain, namely the strain-induced frontogenesis mechanism [Lapeyre et al., 2006]. While the strength of this mechanism is typically characterized by an Eulerian snapshot of the mesoscale strain rate (MSR) [Zhang et al., 2019; Zhang et al., 2021], such snapshots fail to account for the time-integrated nature of the ocean flow. Here, to capture the persistent strain and thereby allow the identification of underlying energetic drivers, we additionally employ an altimeter-derived Lagrangian strain parameter, the finite-time Lyapunov exponent (FTLE) [Samelson et al., 2013], and the mesoscale LCSs are identified as the ridges of the mesoscale FTLE field [Beron-Vera et al., 2008]. On this basis, we obtained direct observational evidence for the co-occurrence of SAR-detected submesoscale eddy and altimeter-based mesoscale LCS (for example, **Fig. 2a, b**). To further examine the generality of this LCS-related occurrence on global scales, we paired each detected submesoscale eddy with the nearest concurrent (same-day) mesoscale LCS. As a result, the resulting 60,702 pairs reveal a previously unquantified spatial relationship that submesoscale eddies dominantly occur near mesoscale LCSs, with 84.60% located at distances less than 10 km (**Fig. 2c**). This pronounced clustering around LCSs suggests that mesoscale LCSs serve as the dominant drivers of submesoscale eddies in the global oceans.

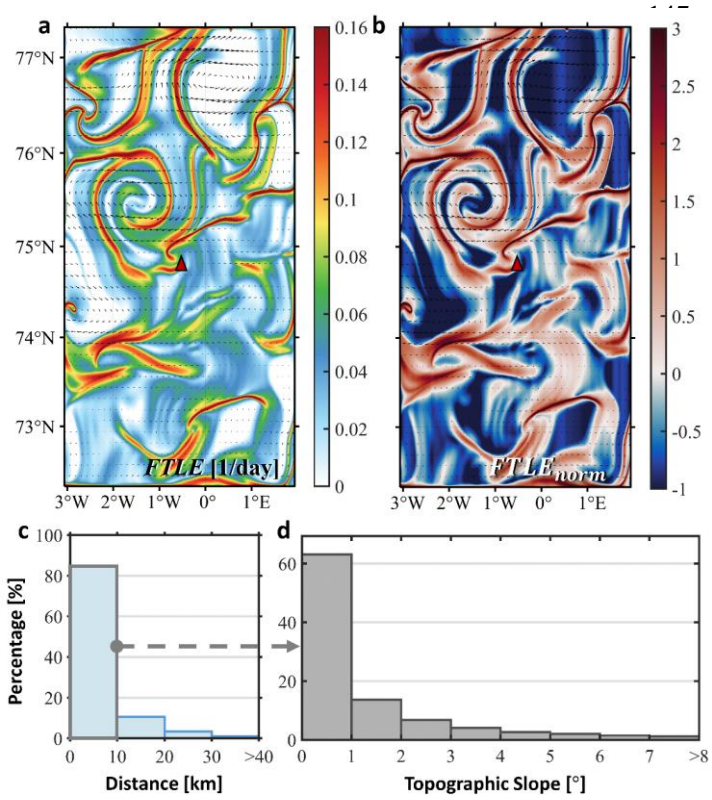


Fig. 2 | Co-occurrence of submesoscale eddies with mesoscale LCSs. a, 5° × 5° mesoscale FTLE field centred on a submesoscale eddy (red triangle in the centre) observed on 4 July, 2018. The vectors show the absolute geostrophic velocity and the ridges of the FTLE field are the mesoscale LCSs. **b**, Corresponding normalized mesoscale FTLE field. **c**, Histogram of the distances of the submesoscale eddies from the mesoscale LCSs. **d**, Topographic slope distribution for submesoscale eddies located within 10 km of the mesoscale LCS.

To illustrate how these LCSs drive the generation of submesoscale eddies, we calculated the strain condition (MSR and FTLE) and energy source (kinetic energy (KE)) quantities for a 5° × 5° region centred around each submesoscale eddy, and

normalized them by the local mean and standard deviation. After this normalization, the regions under the influence of mesoscale LCSs exhibit positive values, whereas areas away from LCSs show negative values (red and blue colours, respectively, in **Fig. 2b**). Moreover, we quantified the spatial variation of these physical quantities with increasing distance from the mesoscale LCSs. The globally averaged values for FTLE, MSR, and KE show a clear spatial decaying trend away from mesoscale LCSs (**Fig. 3**). Additionally, the normalized results show that KE shifts from positive to negative values at distance of roughly 10 km from the LCSs, and at distances shorter than 10 km from the LCSs, both KE and strain are positive (**Fig. 3b**), spatially coinciding with the observed clusters of submesoscale eddies around LCSs (**Fig. 2c**). This coincidence suggests that the energy source and straining preconditions jointly support the generation of submesoscale eddies by strain-induced frontogenesis mechanism. To be more specific, the mesoscale strain field tends to stretch the flow in one direction and compress it in the direction perpendicular to it, thereby generating and continuously sharpening horizontal fronts, a process known as frontogenesis [McWilliams, 2021]. As their extent in the direction of compression decreases, sharpening fronts become unstable and generate submesoscale eddies by triggering a variety of instabilities that develop through extracting kinetic energy from mesoscale processes [Jing et al., 2021; Zhang et al., 2023b]. Notably, in the clustering region of submesoscale eddies, the values of the FTLE (up to 1.2) are significantly higher than those of the MSR (up to 0.2), suggesting that an accumulated strain can more effectively characterize the strain-induced frontogenesis process than a strain snapshot.

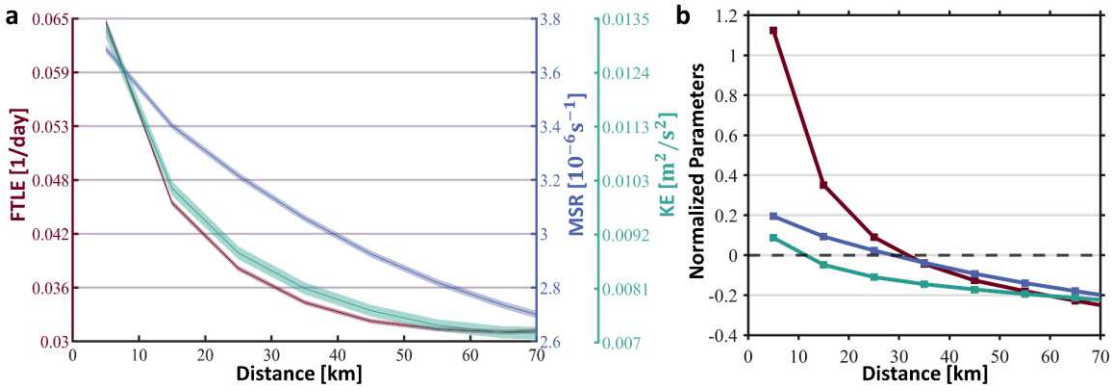


Fig. 3 | Decreasing trend of energy and strain away from mesoscale LCSs. a, Global averaged mesoscale KE (green line), mesoscale FTLE (red line), and MSR (blue line) as functions of the distance from LCSs. All quantities were derived from altimetric velocity fields within a 5° × 5° region centred around submesoscale eddies. The faded strips on each curve indicate the corresponding standard errors. **b**, same as for **a**, but all quantities are normalized by their local mean and standard deviation in the 5° × 5° region.

We noted that the co-occurrences of submesoscale eddies and LCSs were also observed in regions dominated by flow-topography interactions, characterized by topographic slopes steeper than 3° [Gula et al., 2015]. Of all submesoscale eddies generated within 10 km from an LCS, 16.49% were located in such regions (**Fig. 2d**). This finding

not only demonstrates the two-step generation hypothesis proposed by a previous model simulation study [Rosso et al., 2015], that is, the topography controls the mesoscale flow to generate strong strain fields, which in turn drives the generation of submesoscale eddies, but also explicitly identifies that the strong strain is from mesoscale LCSs.

Role of mesoscale eddies

Mesoscale eddies, accounting for approximately 90% of the ocean's total kinetic energy [Ferrari and Wunsch, 2009], are the most ubiquitous and energetic manifestation of mesoscale LCSs. While model simulations identify the edges of mesoscale eddies as hotspots of submesoscale activity [Capuano et al., 2018; McWilliams, 2016], the contribution of the mesoscale eddies to the generation of submesoscale eddies on global scales remains unquantified. To fill this gap, we collocated the SAR-detected submesoscale eddies with mesoscale eddies identified on the same day via satellite altimetry, and investigated their co-occurrences. Considering the irregular shape and varying size of mesoscale eddies, the radial distance from the centre of a mesoscale eddy was normalized by its radius (**Fig. 4a**). Following previously established definitions [Arostegui et al., 2022; Gaube et al., 2019], this normalized radial distance, L_n, was further used to categorize zones inside (core: $L_n \leq 0.5$; periphery: $0.5 < L_n < 2$) and outside ($L_n \geq 2$) the impact of mesoscale eddies. We found that 56% of all submesoscale eddies were inside the influenced zone of 11,824 mesoscale eddies, of which 5,816 were cyclones and 6,008 were anticyclones. Moreover, approximately 10% of submesoscale eddies were located in the cores of mesoscale eddies, and 90% in their peripheries (**Fig. 4b**).

To further illustrate the significant distribution difference, we constructed composite averages of MSR, mesoscale KE and FTLE fields of the collocated (11,824) mesoscale eddies in the normalized mesoscale eddy-centric coordinate (**Methods**). The resulting composite distributions show a distinct ring-shaped belt of normalized positive (enhanced) KE and strain along the eddy edge, whereas the core exhibits negative (suppressed) values (**Fig. 4c-h**). These results demonstrate that the mesoscale eddies create a contrasting dynamical environment: the periphery supplies energy and strain conditions that are preconditions for strain-induced frontogenesis, promoting the generation of submesoscale eddies, in contrast to the unfavourable environment of the core that suppresses submesoscale eddy activity. Furthermore, outside the influenced zone of mesoscale eddies, all quantities decline to near-zero (background) values, further pronouncing the strong negative/positive values in the eddies' core/edge.

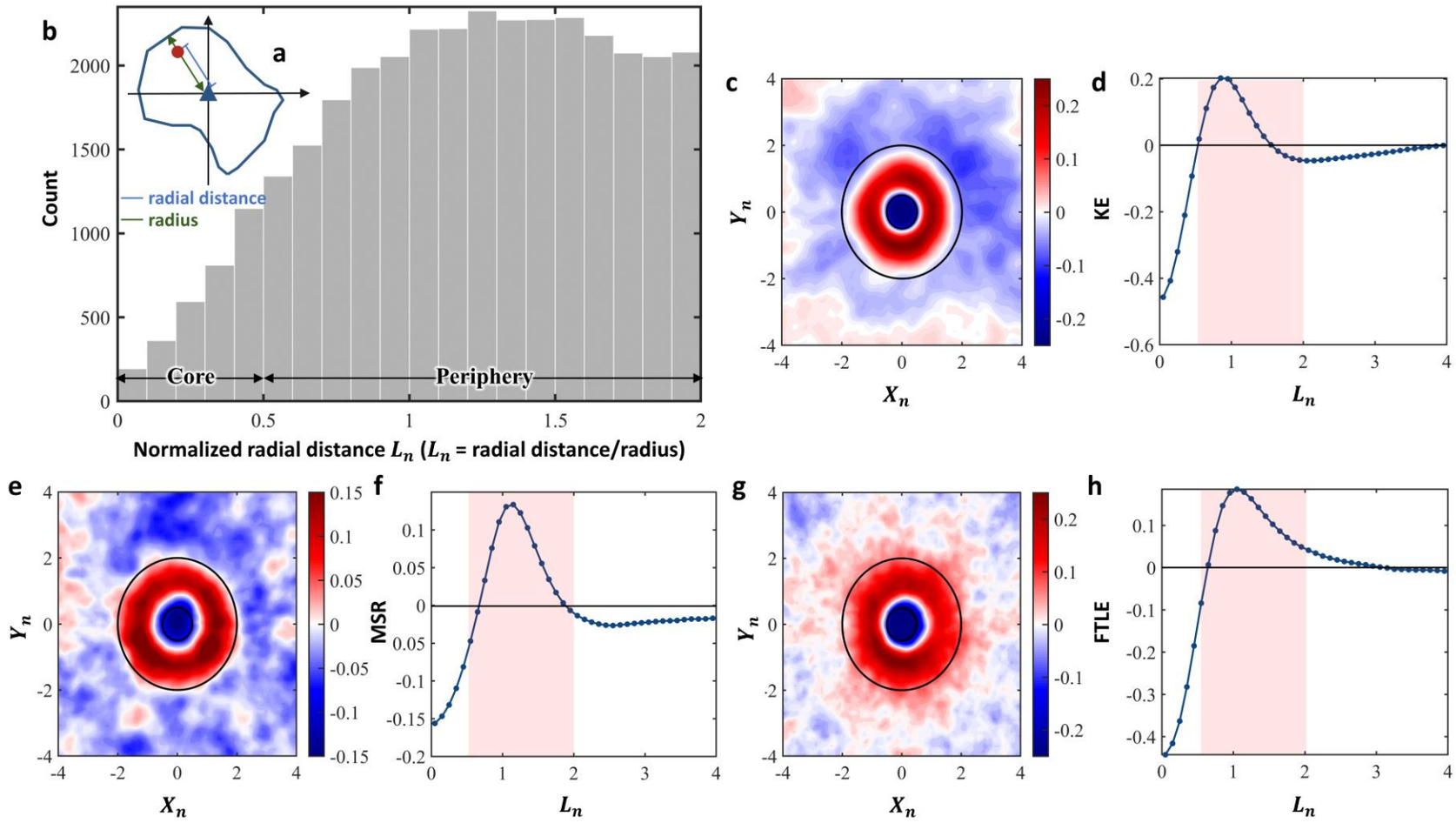


Fig. 4 | Preferred occurrence of submesoscale eddies around mesoscale eddies. a, Schematic of the normalization of the radial distance. The blue contour represents the mesoscale eddy edge, the blue line is the radial distance to a given point (red circle), and the green line is the eddy radius measured along the same radial axis. **b**, Submesoscale eddy count histogram based on normalized radial distance L_n, with the eddy core ($L_n \leq 0.5$) and periphery ($0.5 < L_n < 2$) marked. **c, d,** Composited spatial distribution of the normalized KE in an eddy-centric coordinate system (**c**) and the corresponding radial distribution (**d**). **e, f,** and **g, h,** are the same as **c, d,** but for MSR and FTLE, respectively. The inner and outer circles in the composited spatial distributions indicate the boundaries of the eddy core and periphery, respectively. The red shaded areas in the radial distributions mark the mesoscale eddy periphery. All quantities are normalized by the local mean and standard deviation in the areas of $L_n \leq 4$.

In addition, we examined the role of mixed-layer instability, another important generation mechanism of submesoscale eddies. This mechanism energizes submesoscale eddies by releasing available potential energy stored in the mixed layer, and therefore, its strength can be characterized by the mixed layer depth (MLD) [Callies et al., 2015]. By compositing the MLD of the collocated mesoscale eddies, the resulting composited distribution shows that the modulation of mesoscale eddy on MLD mainly occurs in the area of $L_n < 1$. Within this modulation area, the MLD is reduced in cyclones and enhanced in anticyclones **(Supplementary Fig. 3)**, a pattern also observed in a previous study [Gaube et al., 2019]. If the generation of submesoscale eddies was mainly related to the mixed-layer instability, their occurrences could be expected to be higher in mesoscale anticyclones than in cyclones in the modulation area. However, our results show the opposite: 8,217 submesoscale eddies were detected in cyclones versus 7,102 in anticyclones, indicating mixed-layer instability is not the dominant mechanism. It should be noted that in winter (December, January and February in the Northern Hemisphere and June, July and August in the Southern Hemisphere [Sallée et al., 2021]), when the MLD reaches its seasonal maximum, the occurrences of submesoscale eddies within the modulation region align with the expectation, with 1,729/1,277 eddies detected in anticyclones/cyclones. Overall, although there is a slight shift toward mixed-layer instability-driven generation in winter, it does not alter the conclusion that the generation of global submesoscale eddies primarily depends on strain-induced frontogenesis.

Summary and implications

Characterizing submesoscale eddies has been a challenging task in a systematic fashion due to their kilometer scales, thus hindering our understanding of their driving mechanisms from a global perspective. This study, for the first time, applied global spaceborne SAR data to the ocean submesoscale study, advancing from case and regional studies to a global-scale investigation. Combining the detections of more than 82,000 eddies identified by an automated detection system with concurrent mesoscale LCSs derived from altimeter data, our results show that more than 84% of the submesoscale eddies were observed within 10 km of mesoscale LCSs. A significant decay of both KE and strain with increasing distance from mesoscale LCSs further underscores their connections and highlights the central role of instabilities initiated by the strain-induced frontogenesis in the generation of submesoscale eddies. Our findings show direct evidence that mesoscale LCSs act as the dominant driver of global submesoscale eddy generation, not only validating recent work that potentially links the formation of submesoscale eddies to upper-ocean convergent flows [Yu et al., 2024], but also going a step further in proposing LCSs as an identifiable manifestation of such flows. The remaining submesoscale eddies not associated with LCSs (~16%) may be linked to mesoscale features weaker than the LCS threshold used in this study, to interactions between topography and submesoscale currents [Rosso et al., 2015], and mixed layer instability [Callies et al., 2015]. Additionally, focusing on the most energetic manifestation of LCSs, mesoscale eddies, we found a submesoscale eddy active band

around mesoscale eddy centres, between 0.5 and 2 times their radius. This ring-shaped band hosts more than 50% of all submesoscale eddy occurrences, and it also exhibits high values of both KE and strain that are needed for strain-induced frontogenesis, providing quantitative confirmation of previous simulation findings of enhanced submesoscale processes at the edges of mesoscale eddies [Capuano et al., 2018; McWilliams, 2016].

This study makes a significant contribution by, firstly, accurately revealing the primary driving mechanism of global submesoscale eddies through a synergistic application of remote sensing data, which is needed for the parameterization of submesoscale dynamics in numerical models and opens a practical route to assess their global impact on the ocean energy budget and marine ecosystems. Existing parameterizations of submesoscale processes focused on mixed-layer instability [Fox-Kemper et al., 2008], and more recently, included mesoscale strain rate [Zhang et al., 2023b]. Our findings underscore the dominance of strain-induced frontogenesis, making it necessary to be included in submesoscale parameterizations. More importantly, our results reveal that mesoscale LCSs are the dominant drivers of submesoscale eddies. This implies that the locations of submesoscale eddies are not random but are organized along the mesoscale LCSs, opening up a feasible, LCS-based way to locate submesoscale eddies globally, thereby quantifying their impact on the global vertical exchange of heat and nutrients.

It should be noted that our analyses focused on how a purely mesoscale background field unidirectionally influences the generation of submesoscale eddies, as conventional satellite altimetry cannot resolve submesoscale features. Interactions between submesoscale processes, such as pre-existing submesoscale fronts or filaments that become unstable and generate submesoscale eddies, cannot be resolved in this study. Here, the recently launched Surface Water and Ocean Topography (SWOT) mission offers a unique opportunity to resolve submesoscale dynamics [Ancher et al., 2025], and hence, the synergistic use of SWOT and SAR data will be critical to further investigations of frontogenesis at the submesoscale.

[1] Munk, W., Armi, L., Fischer, K., & Zachariasen, F. (2000). Spirals on the sea. Proceedings of the Royal Society of London. Series A: Mathematical, Physical and Engineering Sciences, 456(1997), 1217-1280.

[2] Su, Z., Wang, J., Klein, P., Thompson, A. F., & Menemenlis, D. (2018). Ocean submesoscales as a key component of the global heat budget. Nature communications, 9(1), 775.

[3] Archer, M., Wang, J., Klein, P., Dibarboure, G., & Fu, L. L. (2025). Wide-swath satellite altimetry unveils global submesoscale ocean dynamics. Nature, 640(8059), 691-696.

[4] Lévy, M., Franks, P. J., & Smith, K. S. (2018). The role of submesoscale currents in structuring marine ecosystems. Nature communications, 9(1), 4758.

[5] Wang, S., Jing, Z., Wu, L., Cai, W., Chang, P., Wang, H., ... & Yang, H. (2022). El Niño/Southern Oscillation inhibited by submesoscale ocean eddies. Nature Geoscience, 15(2), 112-117.

[6] Zhang, Z., Liu, Y., Qiu, B., Luo, Y., Cai, W., Yuan, Q., ... & Tian, J. (2023a). Submesoscale inverse energy cascade enhances Southern Ocean eddy heat transport. Nature Communications, 14(1), 1335.

[7] Chelton, D. B., Schlax, M. G., & Samelson, R. M. (2011). Global observations of nonlinear mesoscale eddies. Progress in oceanography, 91(2), 167-216.
[8] Holloway, G. (1986). Estimation of oceanic eddy transports from satellite altimetry. Nature, 323(6085), 243-244.
[9] Rai, S., Farrar, J. T., & Aluie, H. (2025). Atmospheric wind energization of ocean weather. Nature Communications, 16(1), 1172.
[10] Balwada, D., Xie, J. H., Marino, R., & Feraco, F. (2022). Direct observational evidence of an oceanic dual kinetic energy cascade and its seasonality. Science Advances, 8(41), eabq2566.
[11] Schubert, R., Gula, J., Greatbatch, R. J., Baschek, B., & Biastoch, A. (2020). The submesoscale kinetic energy cascade: Mesoscale absorption of submesoscale mixed layer eddies and frontal downscale fluxes. Journal of Physical Oceanography, 50(9), 2573-2589.
[12] Yu, X., Barkan, R., & Naveira Garabato, A. C. (2024). Intensification of submesoscale frontogenesis and forward energy cascade driven by upper-ocean convergent flows. Nature Communications, 15(1), 9214.
[13] Dong, H., Zhou, M., McWilliams, J. C., Raj, R. P., d'Ovidio, F., Fer, I., ... & Sperrevik, A. K. (2025). Warm rings in mesoscale eddies in a cold straining ocean. Nature Communications, 16(1), 9252.
[14] McWilliams, J. C. (2016). Submesoscale currents in the ocean. Proceedings of the Royal Society A: Mathematical, Physical and Engineering Sciences, 472(2189), 20160117.
[15] Zhang, Z., Zhang, X., Qiu, B., Zhao, W., Zhou, C., Huang, X., & Tian, J. (2021). Submesoscale currents in the subtropical upper ocean observed by long-term high-resolution mooring arrays. Journal of Physical Oceanography, 51(1), 187-206.
[16] Gula, J., Molemaker, M. J., & McWilliams, J. C. (2016). Topographic generation of submesoscale centrifugal instability and energy dissipation. Nat. Commun., 7, 12811.
[17] Johannessen, J. A., Shuchman, R. A., Digranes, G., Lyzenga, D. R., Wackerman, C., Johannessen, O. M., & Vachon, P. W. (1996). Coastal ocean fronts and eddies imaged with ERS 1 synthetic aperture radar. Journal of Geophysical Research: Oceans, 101(C3), 6651-6667.
[18] Callies, J., Ferrari, R., Klymak, J. M., & Gula, J. (2015). Seasonality in submesoscale turbulence. Nature communications, 6(1), 6862.
[19] Lapeyre, G., Klein, P., & Hua, B. L. (2006). Oceanic restratification forced by surface frontogenesis. Journal of Physical Oceanography, 36(8), 1577-1590.
[20] Rosso, I., Hogg, A. M., Kiss, A. E., & Gayen, B. (2015). Topographic influence on submesoscale dynamics in the Southern Ocean. Geophysical Research Letters, 42(4), 1139-1147.
[21] Stuhlmacher, A., Gade, M., 2020. Statistical analyses of eddies in the Western Mediterranean Sea based on Synthetic Aperture Radar imagery. Remote Sens. Environ. 250, 112023.
[22] Srinivasan, K., McWilliams, J. C., Renault, L., Hristova, H. G., Molemaker, J., & Kessler, W. S. (2017). Topographic and mixed layer submesoscale currents in the near-surface southwestern tropical Pacific. Journal of Physical Oceanography, 47(6), 1221-1242.
[23] Chen, G., & Han, G. (2019). Contrasting short-lived with long-lived mesoscale eddies in the global ocean. Journal of Geophysical Research: Oceans, 124(5), 3149-3167.
[24] Beron-Vera, F. J., Olascoaga, M. J., & Goni, G. J. (2008). Oceanic mesoscale eddies as revealed by Lagrangian coherent structures. Geophysical Research Letters, 35(12).
[25] Prants, S. V., Budyansky, M. V., & Uleysky, M. Y. (2014). Identifying Lagrangian fronts with favourable fishery conditions. Deep Sea Research Part I: Oceanographic Research Papers, 90, 27-35.
[26] Tian, F., Wang, M., Liu, X., He, Q., & Chen, G. (2022). SLA-based orthogonal parallel detection of

371 global rotationally coherent Lagrangian vortices. Journal of Atmospheric and Oceanic Technology, 39(6),
372 823-836.
373 [27] Peacock, T., & Haller, G. (2013). Lagrangian coherent structures: The hidden skeleton of fluid flows.
374 Physics today, 66(2), 41-47.
375 [28] Beron-Vera, F. J., Wang, Y., Olascoaga, M. J., Goni, G. J., & Haller, G. (2013). Objective detection
376 of oceanic eddies and the Agulhas leakage. Journal of Physical Oceanography, 43(7), 1426-1438.
377 [29] Liu, T., & Abernathey, R. (2022). A global Lagrangian eddy dataset based on satellite altimetry.
378 Earth System Science Data Discussions, 2022, 1-20.
379 [30] Bashmachnikov, I. L., Kozlov, I. E., Petrenko, L. A., Glok, N. I., & Wekerle, C. (2020). Eddies in
380 the North Greenland Sea and Fram Strait from satellite altimetry, SAR and high-resolution model data.
381 Journal of Geophysical Research: Oceans, 125(7), e2019JC015832.
382 [31] Zi, N., Li, X. M., Gade, M., Fu, H., & Min, S. (2024). Ocean eddy detection based on YOLO deep
383 learning algorithm by synthetic aperture radar data. Remote Sensing of Environment, 307, 114139.
384 [32] Zi, N., Li, X. M., Yuan, H., & Cai, K. (2025). Deep learning for eddy detection in the Arctic marginal
385 ice zone by spaceborne SAR. IEEE Journal of Selected Topics in Applied Earth Observations and Remote
386 Sensing.
387 [33] Johannessen, O. M., Johannessen, J. A., Svendsen, E., Shuchman, R. A., Campbell, W. J., &
388 Josberger, E. (1987). Ice-edge eddies in the Fram Strait marginal ice zone. Science, 236(4800), 427-429.
389 [34] Karimova, S. (2012). Spiral eddies in the Baltic, Black and Caspian seas as seen by satellite radar
390 data. Advances in Space Research, 50(8), 1107-1124.
391 [35] Mkhinini, N., Coimbra, A. L. S., Stegner, A., Arsouze, T., Taupier-Letage, I., & Béranger, K. (2014).
392 Long-lived mesoscale eddies in the eastern Mediterranean Sea: Analysis of 20 years of AVISO
393 geostrophic velocities. Journal of Geophysical Research: Oceans, 119(12), 8603-8626.
394 [36] Zatsepin, A. G., Ginzburg, A. I., Kostianoy, A. G., Kremenetskiy, V. V., Krivosheya, V. G., Stanichny,
395 S. V., & Poulain, P. M. (2003). Observations of Black Sea mesoscale eddies and associated horizontal
396 mixing. Journal of Geophysical Research: Oceans, 108(C8).
397 [37] McWilliams, J. C. (1985). Submesoscale, coherent vortices in the ocean. Reviews of Geophysics,
398 23(2), 165-182.
399 [38] Schaeffer, A., Gramoulle, A., Roughan, M., & Mantovanelli, A. (2017). Characterizing frontal
400 eddies along the East Australian Current from HF radar observations. Journal of Geophysical Research:
401 Oceans, 122(5), 3964-3980.
402 [39] Zhang, Z., Qiu, B., Klein, P., & Travis, S. (2019). The influence of geostrophic strain on oceanic
403 ageostrophic motion and surface chlorophyll. Nature Communications, 10(1), 2838.
404 [40] Samelson, R. M. (2013). Lagrangian motion, coherent structures, and lines of persistent material
405 strain. Annual review of marine science, 5(1), 137-163.
406 [41] McWilliams, J. C. (2021). Oceanic frontogenesis. Annual Review of Marine Science, 13(1), 227-
407 253.
408 [42] Jing, Z., Fox-Kemper, B., Cao, H., Zheng, R., & Du, Y. (2021). Submesoscale fronts and their
409 dynamical processes associated with symmetric instability in the northwest Pacific subtropical ocean.
410 Journal of Physical Oceanography, 51(1), 83-100.
411 [43] Zhang, J., Zhang, Z., & Qiu, B. (2023b). Parameterizing submesoscale vertical buoyancy flux by
412 simultaneously considering baroclinic instability and strain-induced frontogenesis. Geophysical
413 Research Letters, 50(8), e2022GL102292.
414 [44] Gula, J., Molemaker, M. J., & McWilliams, J. C. (2015). Topographic vorticity generation,

submesoscale instability and vortex street formation in the Gulf Stream. Geophysical Research Letters, 42(10), 4054-4062.
[45] Ferrari, R., & Wunsch, C. (2009). Ocean circulation kinetic energy: Reservoirs, sources, and sinks. Annual Review of Fluid Mechanics, 41(1), 253-282.
[46] Capuano, T. A., Speich, S., Carton, X., & Blanke, B. (2018). Mesoscale and submesoscale processes in the Southeast Atlantic and their impact on the regional thermohaline structure. Journal of Geophysical Research: Oceans, 123(3), 1937-1961.
[47] Arostegui, M. C., Gaube, P., Woodworth-Jefcoats, P. A., Kobayashi, D. R., & Braun, C. D. (2022). Anticyclonic eddies aggregate pelagic predators in a subtropical gyre. Nature, 609(7927), 535-540.
[48] Gaube, P., J. McGillicuddy Jr, D., & Moulin, A. J. (2019). Mesoscale eddies modulate mixed layer depth globally. Geophysical Research Letters, 46(3), 1505-1512.
[49] Sallée, J. B., Pellichero, V., Akhoudas, C., Pauthenet, E., Vignes, L., Schmidtko, S., ... & Kuusela, M. (2021). Summertime increases in upper-ocean stratification and mixed-layer depth. Nature, 591(7851), 592-598.
[50] Fox-Kemper, B., Ferrari, R., & Hallberg, R. (2008). Parameterization of mixed layer eddies. Part I: Theory and diagnosis. Journal of Physical Oceanography, 38(6), 1145-1165.

Methods

SAR data

We used C-band spaceborne SAR imagery from the Copernicus S1 mission operated by the European Space Agency (ESA). The images originate from the dual-satellite constellation, S1A and S1B, which together provide near-global ocean coverage every 6 days. Our data consist of horizontally (HH) or vertically (VV) polarized data acquired in Interferometric Wide Swath (IW), Extra-Wide Swath (EW), and Wave (WV) modes. The IW mode serves as the primary operational mode in the offshore regions, providing a pixel spacing of 10 m and a swath width of 250 km. In the polar zones, the EW mode is the main acquisition mode, offering 40 m pixel spacing and 410 km swath width. WV mode is the default mode over the open ocean, with small stripmap scenes every 100 km along the satellite track, each covering an area of 20 km by 20 km with a pixel spacing of 5 m. We used the Ground Range Detected (GRD) Level-1 products for IW/EW modes, and the Single Look Complex (SLC) product for WV mode. Moreover, in sea areas with sparse or no acquisition of S1 data, we additionally used Advanced SAR (ASAR) data from the EnviSat mission, which had a 35-day repeat cycle and whose Wide Swath Mode (WSM) provided data at HH or VV polarization, with a swath width of 405 km and a pixel spacing of 75 m.

To enhance the visibility of eddies, the SAR data were pre-processed, with steps including radiometric calibration, speckle filtering, land masking, log transformation, and geocoding **[Zi et al., 2024]**. To reduce the computational effort for pre-processing, we visually inspected all quicklooks of SAR data in IW/EW mode and selected those containing eddies (with a high tolerance of look-alikes). This resulted in a final collection of 28,742 S1 EW/IW scenes from 2018 (**Supplementary Fig. 1a**), 5,798 EnviSat WSM SAR scenes from its entire operational period (2002-2012; **Supplementary Fig. 1b**), and all available (3,160,608) S1 WV scenes from 2018 and

2019 (**Supplementary Fig. 1c**). Noted that our objective was to detect a sufficient amount of submesoscale eddies globally in support of our global mechanism analysis, rather than to determine their global distribution patterns. To this end, we used data from two spaceborne SAR missions, despite their different operating times, to achieve near-global coverage (**Fig. 1a**).

Altimetry data and mesoscale eddy product

The multi-satellite level-4 gridded altimetry product, generated by Data Unification and Altimeter Combination System (DUACS) on a 0.125° grid, was obtained from the Copernicus Marine Service. We used daily absolute geostrophic velocity and geostrophic velocity anomaly data temporally aligned with the acquisition period of the SAR data.

The mesoscale eddy product, Mesoscale Eddy Trajectory Atlas version 3.2 (META 3.2), provides daily mesoscale eddies from January 1993 to March 2020 and is available from the Archiving, Validation and Interpretation of Satellite Oceanographic (AVISO) database. This dataset includes the centre, radius, and edge contour of each eddy, where the eddy centre and radius are defined as those of the best-fit circle corresponding to the contour of maximum circum-average speed (defined as the eddy edge) [Pegliasco et al., 2022]. In this study, in cases when the eddy centre was outside its edge, the geometric centroid of the edge contour was used as the eddy centre.

To compensate for the mesoscale eddies potentially missed in the META 3.2 dataset due to its strict eddy identification criteria [Mason et al., 2014], a vector geometry-based eddy detection algorithm was applied [Nencioli et al., 2010]. This algorithm identifies mesoscale eddies by applying constraints to the distribution characteristics of velocity vectors around the eddy centre, where the constraints are derived from the general features of the velocity fields in the presence of eddies. We used a 10° × 10° DUACS absolute geostrophic velocity field centred on each submesoscale eddy as the input. The choice of this extent was based on the eddy sizes, with over 90% of the global mesoscale eddies having diameters ranging from 100 km to 300 km [Chelton et al., 2011]. This ensured a sufficient coverage for mesoscale eddy identification, and consequently, we identified 13,449 eddies missed in the META 3.2 dataset.

Submesoscale eddy detection by SAR

We detected ocean eddies on SAR images using a previously proposed eddy detection system named EOLO [Zi et al., 2024]. Briefly, building upon the architecture of the You-Only-Look-Once (YOLO) deep learning algorithm, EOLO introduced attention mechanisms to focus on the key (eddy) features on SAR imagery, and it adopted an up-sampling operator with a large receptive field to preserve fine details on the high-resolution SAR images. To facilitate multi-scale eddy detection on full SAR scenes, EOLO employed a slicing-aided inference technique, and to extract geographic locations and diameters of eddy detections, EOLO further combined the geographic affine transformation. It should be noted that EOLO uses horizontal (non-rotated) detection boxes, with the eddy diameter calculated as the average of the box width and height, and the mean error caused by the horizontal detection box was estimated to be

499 less than 2% [Zi et al., 2024].

500 After iterative training on a dataset comprising 2,541 eddy samples, EOLO yielded
501 a precision of 90.5% and a recall of 87.3% (precision/recall of 100% indicates 0
502 false/miss detection). EOLO's generalization was further evaluated using 820 SAR
503 scenes containing various/complex ocean conditions acquired in different seas, with a
504 precision and recall of more than 95% and 85%, respectively. Furthermore, by applying
505 EOLO on 6,315 SAR scenes acquired over the Western Mediterranean Sea, the spatial
506 distribution of detected eddies showed high consistency with previous studies [Karimova
507 and Gade, 2016; Stuhlmacher and Gade, 2020], with a detection precision of about 96% [Zi et al., 2024].

508 Eddies with a radius smaller than the local R_d are defined as submesoscale eddies
509 [McWilliams, 1985; Schaeffer et al., 2017; Bashmachnikov et al., 2020]. Although a global 1 ° gridded R_d
510 atlas from Chelton et al. [Chelton et al., 1998] is publicly available, it focuses on the open
511 ocean and lacks coverage of regions with water depths shallower than 3500 m.
512 Therefore, following their method, we calculated R_d for the World's oceans as

513 $$R_d = \frac{1}{\pi|f(\theta)|}\int_{-H}^{0} N(z)dz \;\; ; \;\; |\theta| \geq 5^{\circ}$$

514 and

515 $$R_d = \sqrt{\frac{1}{|2\pi\beta(\theta)|}\int_{-H}^{0} N(z)dz} \;\; ; \;\; |\theta| < 5^{\circ}$$

516 where θ is latitude, $f(\theta) = 2\Omega sin\theta$ is the Coriolis parameter and $\beta(\theta) =$
517 $df/dy = 2\Omega\alpha^{-1}cos\theta$ is its latitudinal gradient, Ω is Earth's angular velocity, α is
518 the Earth's radius, and H is the water depth. The buoyancy frequency $N(z)$ is derived
519 using the Gibbs SeaWater (GSW) Oceanographic Toolbox [McDougall et al., 2011], by first
520 calculating conservative temperature Θ and absolute salinity S_A using in-situ
521 temperature and practical salinity from World Ocean Atlas 2018 (WOA18), and then
522 interpolating Θ and S_A to a 10 m vertical resolution.

523 **FTLE-based LCS detection by radar altimeter**

524 Among various LCS detection approaches, the FTLE-based method provides a notable
525 advantage in identifying LCSs within complex ocean flow fields [Beron-Vera et al., 2008; Tew
526 Kai et al., 2009]. The FTLE quantifies the strain rate between trajectories over a selected
527 time interval [Samelson et al., 2013] and is typically derived from discrete velocity field data.
528 Here, we calculated it using the DUACS geostrophic velocity field $\mathbf{v}$. To remove large-
529 scale signals unrelated to mesoscale dynamics, the velocity fields were high-pass
530 filtered using a Gaussian filter with a half-power cutoff wavelength of 10° [Ni et al., 2020].
531 The resulting velocity field is given by $\mathbf{v}(\mathbf{x}, t) = (u(\mathbf{x}, t), v(\mathbf{x}, t))$. The computation
532 of FTLE begins by mapping the trajectory of a set of fluid particles, described by the
533 transformation

534 $$\mathbf{F}_{t_0}^{t_1} : \mathbf{x}_0 \rightarrow \mathbf{x}_1(t; \mathbf{x}_0), \;\; t \in [t_0, t_1],$$

535 where $\mathbf{x}_1$ is obtained by solving $d\mathbf{x}/dt = \mathbf{v}(\mathbf{x}, t)$, $\mathbf{x}(t_0) = \mathbf{x}_0 = (x0, y0)$ at the time
536 $t = t_1$. This transformation maps fluid particles from their initial positions $\mathbf{x}_0$ to their

final positions $\mathbf{x}_1$. Then, the Cauchy-Green deformation tensor is calculated as $\mathbf{C} = (\nabla\mathbf{F})^T\nabla\mathbf{F}$ to quantify time-dependent deformation of fluid parcels, where

$$\nabla\mathbf{F}_{t_0}^{t_1}(\mathbf{x}_0) = \begin{bmatrix} \frac{\partial x_1}{\partial x_0} & \frac{\partial x_1}{\partial y_0} \\ \frac{\partial y_1}{\partial x_0} & \frac{\partial y_1}{\partial y_0} \end{bmatrix}.$$

Finally, the FTLE, $\sigma(\mathbf{x}, t_0, t_1)$, is computed from the largest eigenvalue of $\mathbf{C}$, denoted by λ_{max}:

$$\sigma(\mathbf{x}_0, t_0, t_1) = \left| \frac{1}{|t_1 - t_0|} \ln\left(\sqrt{\lambda_{max}[\mathbf{C}(\mathbf{x}_0, t_0, t_1)]}\right) \right|,$$

where t_0 is the date when the eddy was observed by SAR, and t_1 is set to 30 days prior to t_0. The choice of a 30-day integration window has been shown to be sufficient to resolve mesoscale LCSs [Beron-Vera et al., 2010]. Furthermore, the FTLE was produced on grids with a resolution 15 times finer than the velocity grid to obtain finer ridge lines [Onu et al., 2015]. To accelerate the calculation, FTLE fields were calculated within a 5° × 5° area centred on each submesoscale eddy. LCSs are then identified as ridges within these fields [Shadden et al., 2005; Beron-Vera et al., 2008], defined by a threshold set at the 90th percentile of FTLE values [Veatch et al., 2025].

Environmental and dynamical quantities

The bottom topographic slope is calculated as $tan^{-1}\nabla h$, where h is the bathymetry extracted from the General Bathymetric Chart of the Oceans (GEBCO) dataset with a spatial resolution of 15 arcsec.

The MLD was obtained from the daily CMEMS Global Ocean Physics Reanalysis product, with a spatial resolution of 0.083°. It is defined as the depth where the density increase compared to the density at 10-m depth corresponds to a 0.2°C decrease in temperature in local surface conditions.

The MSR is commonly employed as the metric to quantify the strength of strain-induced frontogenesis [McWilliams, 2021; Zhang et al., 2023a; Lapeyre et al., 2006], and was calculated as

$$MSR = \sqrt{\left(\frac{\partial u}{\partial x} - \frac{\partial v}{\partial y}\right)^2 + \left(\frac{\partial u}{\partial y} + \frac{\partial v}{\partial x}\right)^2}.$$

The mesoscale kinetic energy is used to characterize the kinetic energy of mesoscale currents and is computed as $KE = (u^2 + v^2)/2$.

Distance analysis

The distance analysis is applied to investigate the spatial variation of energy source (KE) and strain (MSR and FTLE) with increasing distance to mesoscale LCSs. This analysis was applied to fields of KE, MSR, and FTLE computed within a 5° × 5° domain centred on each submesoscale eddy. To remove the influence of regional differences, these dynamical quantities are normalized with the local mean and standard deviation [Zhang and Qiu, 2018], e.g., $KE_{norm} = (KE - KE_{mean})/KE_{std}$. Then, for each grid cell, we calculated the distance to the nearest LCS and grouped the corresponding quantity values into 10

573 km bins. Finally, the bin-averaged values for each quantity were obtained (**Fig. 3**).
574 Given the original 0.125° resolution of the velocity data for LCS identification, a 10
575 km bin was adopted for our statistical analysis.

576 **Composition in mesoscale eddy-centric coordinate**

577 The composition analysis projects dynamical quantities to the mesoscale eddy-centric
578 coordinate to characterize their spatial variation around the eddy centre. We first
579 identified co-occurring pairs of each submesoscale eddy and its spatially nearest
580 mesoscale eddy, observed on the same day. To reduce the influence of asymmetric eddy
581 structures, we re-defined the mesoscale eddy radius (R_m) as the distance from the eddy
582 centre to its boundary point, with the radial axis passing through the given grid point
583 (**Fig. 4a**). Only mesoscale eddies containing at least one submesoscale eddy within 2
584 R_m remained for population, and reduplicated mesoscale eddies (i.e., those associated
585 with multiple submesoscale eddies) were removed. Although this selection criterion
586 may bias the mesoscale eddy population toward 'submesoscale-eddy-active' mesoscale
587 eddies, it is reasonable for understanding the preferred distribution patterns of
588 submesoscale eddies under the influence of mesoscale eddies (**Fig. 4**). The dynamical
589 quantities were computed in the 4 R_m region of each mesoscale eddy and were
590 normalized with the local mean and standard deviation. Then, the normalized quantities
591 were projected to the mesoscale eddy-centric coordinate: given the gridded location of
592 the quantity field as (x, y) and its corresponding mesoscale eddy centre as (x_c, y_c),
593 the normalized projected gridded location (x_n, y_n) was obtained as $x_n = (x -$
594 $x_c)/R_m$ and $y_n = (y - y_c)/R_m$. Note that the composition analysis in this study was
595 done without hemisphere segregation to investigate the globally unified patterns, given
596 the well-documented similarity in dynamic structures between the two hemispheres
597 **[Zhang and Qiu, 2018; Zhang et al., 2019]**.

598 # Data Availability

599 S1 SAR data are available from the Alaska Satellite Facility Distributed Active Archive
600 Center website at https://search.asf.alaska.edu/#/. EnviSat ASAR data were obtained
601 from the ESA online catalogue website at https://esar-
602 ds.eo.esa.int/oads/access/collection. The DUACS gridded products and MLD data are
603 publicly available from CMEMS at https://marine.copernicus.eu/. The mesoscale eddy
604 product is accessible from https://aviso.altimetry.fr/. The WOA18 data is available at
605 https://www.ncei.noaa.gov/products/world-ocean-atlas. GEBCO bathymetry data is
606 available from https://www.gebco.net/data-products/gridded-bathymetry-data.

607 # Code availability

608 The code used for generating the figures in this paper is available from the
609 corresponding author upon request.
610
611 [51] Pegliasco, C. et al. META3.1exp: a new global mesoscale eddy trajectory atlas derived from

altimetry. Earth Syst. Sci. Data 14, 1087–1107 (2022).
[52] Mason, E., Pascual, A., & McWilliams, J. C. (2014). A new sea surface height–based code for oceanic mesoscale eddy tracking. Journal of atmospheric and oceanic technology, 31(5), 1181-1188.
[53] Nencioli, F., Dong, C., Dickey, T., Washburn, L., & McWilliams, J. C. (2010). A vector geometry-based eddy detection algorithm and its application to a high-resolution numerical model product and high-frequency radar surface velocities in the Southern California Bight. Journal of atmospheric and oceanic technology, 27(3), 564-579.
[54] Karimova, Svetlana, and Martin Gade. "Eddies in the Western Mediterranean seen by spaceborne radar." 2016 IEEE International Geoscience and Remote Sensing Symposium (IGARSS). IEEE, 2016.
[55] Chelton, D. B., DeSzoeke, R. A., Schlax, M. G., El Naggar, K., & Siwertz, N. (1998). Geographical variability of the first baroclinic Rossby radius of deformation. Journal of Physical Oceanography, 28(3), 433-460.
[56] McDougall, T. J. & Barker, P. M. Getting Started with TEOS-10 and the Gibbs Seawater (GSW) Oceanographic Toolbox (SCOR/IAPSO WG127, 2011).
[57] Tew Kai, E., Rossi, V., Sudre, J., Weimerskirch, H., Lopez, C., Hernandez-Garcia, E., ... & Garçon, V. (2009). Top marine predators track Lagrangian coherent structures. Proceedings of the National Academy of Sciences, 106(20), 8245-8250.
[58] Ni, Q., Zhai, X., Wang, G., & Hughes, C. W. (2020). Widespread mesoscale dipoles in the global ocean. Journal of Geophysical Research: Oceans, 125(10), e2020JC016479.
[59] Beron-Vera, F. J., Olascoaga, M. J., & Goni, G. J. (2010). Surface ocean mixing inferred from different multisatellite altimetry measurements. Journal of physical oceanography, 40(11), 2466-2480.
[60] Onu, K., Huhn, F., & Haller, G. (2015). LCS Tool: A computational platform for Lagrangian coherent structures. Journal of Computational Science, 7, 26-36.
[61] Shadden, S. C., Lekien, F., & Marsden, J. E. (2005). Definition and properties of Lagrangian coherent structures from finite-time Lyapunov exponents in two-dimensional aperiodic flows. Physica D: Nonlinear Phenomena, 212(3-4), 271-304.
[62] Veatch, J. M., Roarty, H., Oliver, M. J., Fredj, E., & Kohut, J. T. (2025). Attractive Lagrangian features in the Mid‐Atlantic bight: Using Lagrangian coherent structures to describe seasonal and interannual changes in circulation. Journal of Geophysical Research: Oceans, 130(10), e2025JC022447.
[63] Zhang, Z., & Qiu, B. (2018). Evolution of submesoscale ageostrophic motions through the life cycle of oceanic mesoscale eddies. Geophysical Research Letters, 45(21), 11-847.

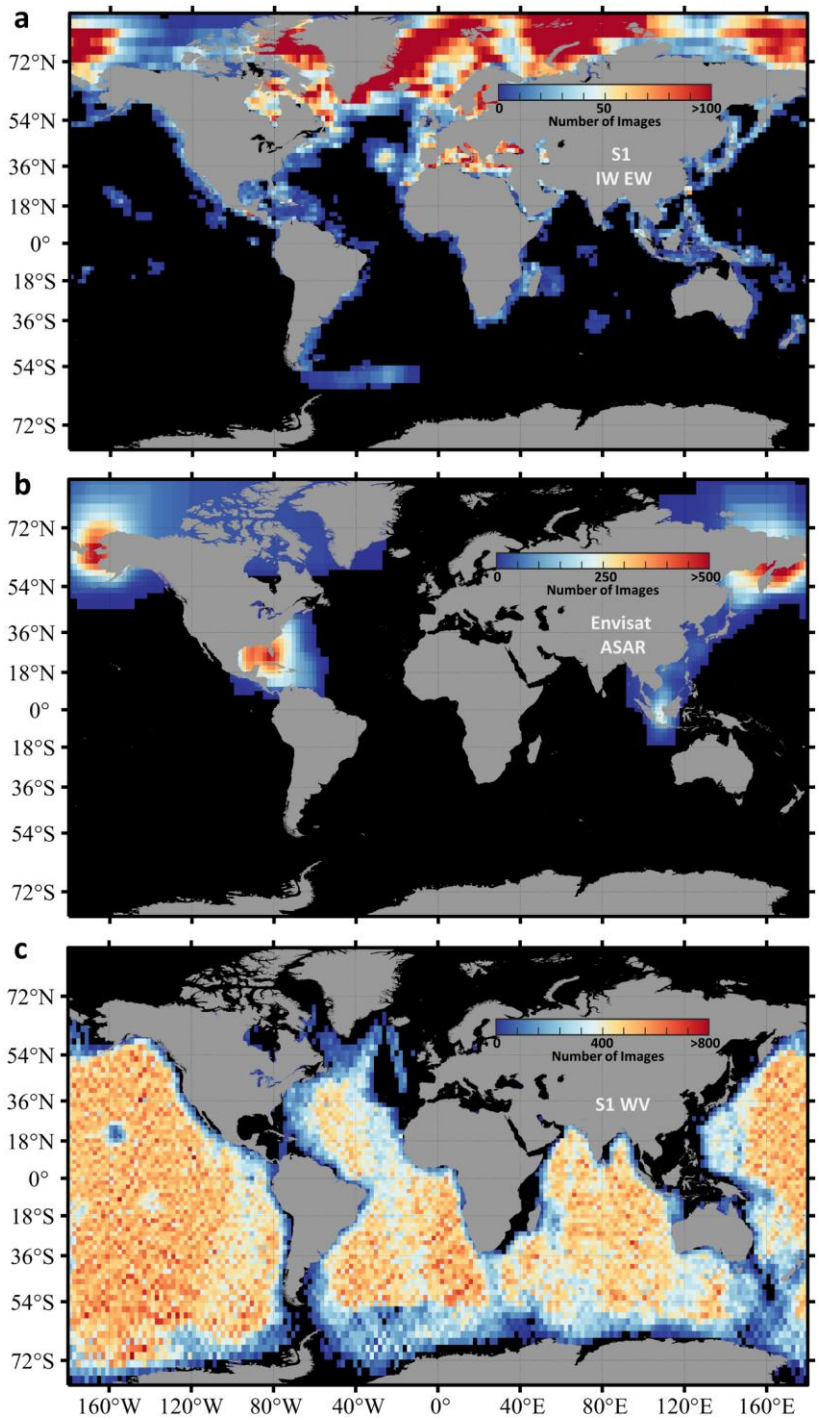
Acknowledgements

This study was supported by the National Science Fund for Distinguished Young Scholars (42025605), and National Natural Science Foundation of China (42225602 and 42530403).

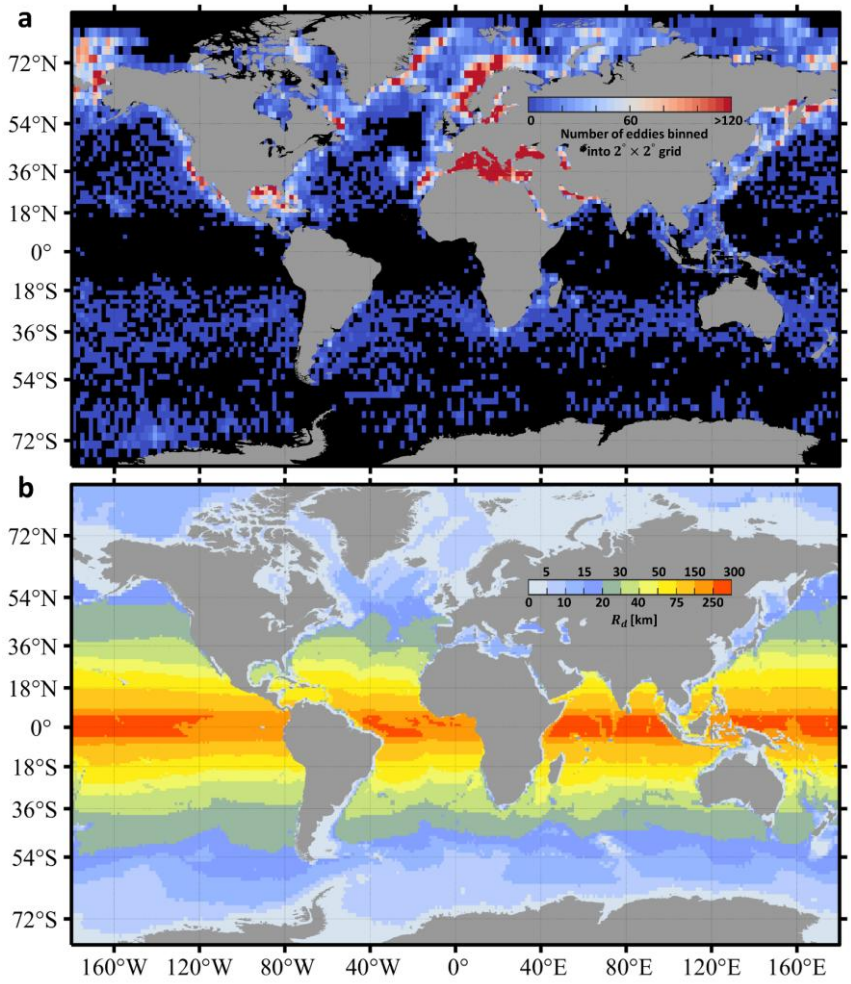
Author contributions

X.-M.L. and N.Z. conceived the study. N.Z. conducted the analysis and drafted the manuscript. N.Z., X.-M.L., G.C., M.G., Z.Z., C.W., J.L., and Z.J. contributed to the results interpretation and manuscript revision.

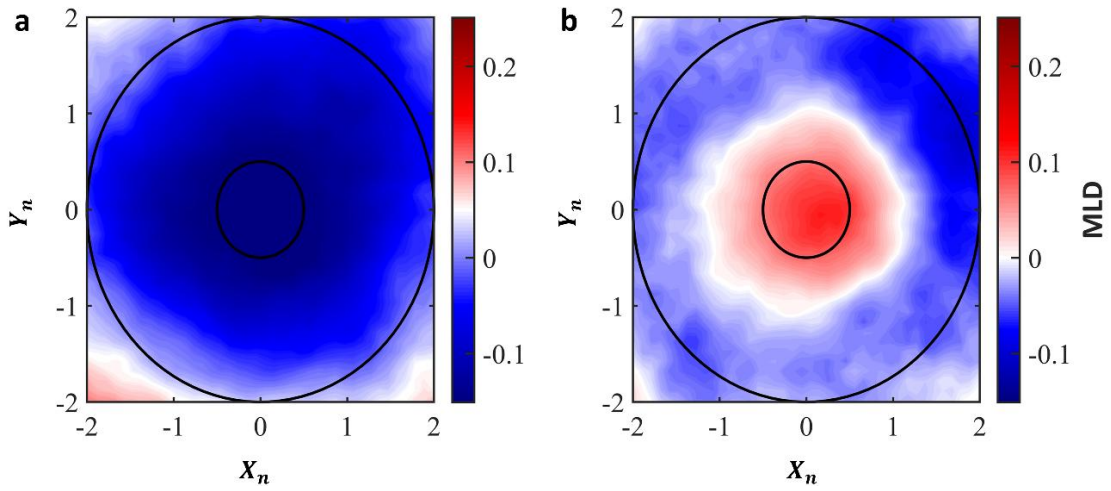
Supplementary Materials



Supplementary Fig. 1. Global distribution of collected SAR data, counted on a 2° × 2° grid. **a,** S1 SAR imagery in IW and EW mode collected in 2018, covering the Arctic Ocean and most coastal waters. **b**, EnviSat ASAR imagery collected in 2002-2012 over the sea areas with only sparse or no coverage of S1 IW and EW mode data, providing a complementary dataset for coastal waters. **c**, The S1 SAR WV mode data collected in 2018 and 2019, covering most of the open oceans.



Supplementary Fig. 2. Global spatial distribution of sub-mesoscale eddies and the first baroclinic Rossby radius of deformation. a, Global distribution of sub-mesoscale eddies detected by SAR binned into a 2° × 2° grid. **b**, Global values of the first baroclinic Rossby radius of deformation (R_d).



Supplementary Fig. 3. Spatial variation of normalized MLD in the mesoscale eddy-centric coordinate. a, Composite distribution for cyclones. **b,** Same as for **a**, but for anticyclones. The inner and outer circles denote the boundaries of the eddy's core and periphery, respectively. The composite method is consistent with that used for dynamical quantities.